EXPERIMENTAL

Klaus Kurt Gast
Wolfgang G. Schreiber
Annette Herweling
Frank Lehmann
Gabor Erdös
Joerg Schmiedeskamp
Hans-Ulrich Kauczor
Balthasar Eberle

Two-dimensional and three-dimensional oxygen mapping by ^{3}He-MRI validation in a lung phantom

K. K. Gast (✉) · W. G. Schreiber ·
A. Herweling · F. Lehmann · G. Erdös ·
J. Schmiedeskamp · H.-U. Kauczor ·
B. Eberle
Department of Radiology,
Johannes Gutenberg University Hospital,
Langenbeckstrasse 1,
55131 Mainz, Germany
e-mail: kgast@radiologie.klinik.uni-mainz.de
Tel.: +49-6131-174056
Fax: +49-6131-173423

Abstract The aim of this study was to validate oxygen-sensitive ^{3}He-MRI in noninvasive determination of the regional, two- and three-dimensional distribution of oxygen partial pressure. In a gas-filled elastic silicon ventilation bag used as a lung phantom, oxygen sensitive two- and three-dimensional ^{3}He-MRI measurements were performed at different oxygen concentrations which had been equilibrated in a range of normal and pathologic values. The oxygen partial pressure distribution was determined from ^{3}He-MRI using newly developed software allowing for mapping of oxygen partial pressure. The reference bulk oxygen partial pressure inside the phantom was measured by conventional respiratory gas analysis. In two-dimensional measurements, image-based and gas-analysis results correlated with $r=0.98$; in three-dimensional measurements the between-methods correlation coefficient was $r=0.89$. The signal-to-noise ratio of three-dimensional measurements was about half of that of two-dimensional measurements and became critical (below 3) in some data sets. Oxygen-sensitive ^{3}He-MRI allows for noninvasive determination of the two- and three-dimensional distribution of oxygen partial pressure in gas-filled airspaces.

Keywords Oxygen · ^{3}He magnetic resonance imaging · Validation · Lung

Introduction

^{3}He-MRI has been shown to be a sensitive technique for functional imaging of the lung [1–4] and could have broader application by distribution of the hyperpolarized gas [5]. In contrast to other lung imaging modalities like computed tomography [6], it does not rely on morphologic visualization of lung parenchyma. Instead, the hyperpolarized gas filling the pulmonary airspace exhibits high and homogeneous signal intensity in normal lungs [7, 8]. The presence of ventilation defects is a characteristic finding in a variety of lung diseases [9].

The presence of paramagnetic molecular oxygen in the alveolar gas shortens T1 of inhaled hyperpolarized ^{3}He. T1-shortening is proportional to ambient oxygen partial pressure (PO_2), which then can be determined by T1-weighted measurements of hyperpolarized ^{3}He ($P_{He}O_2$) [10].

Previous studies used imaging sequences without slice selection [11]. These sequences yield sufficient in-plane resolution, but there is a lack of spatial resolution in the direction perpendicular to the imaged plane. $P_{He}O_2$ measurements using such imaging sequences have been validated by results of respiratory gas analyzers [12]. In slice-selective 2D imaging, diffusive ^{3}He exchange between excited and unexcited slices systematically "blurs" regional oxygen measurements depending, inter alia, on slice thickness [11]. More recent developments in sequence design now also allow the generation of 3D data sets, exciting all spins within the imaged volume simultaneously and thus avoiding measurement-induced polarization gradients. The current study intends to perform the first validation of a 3D oxygen-sensitive ^{3}He-MRI sequence in a lung phantom and to compare it with a 2D sequence as validated before.

Methods

Imaging

Gas polarization and packaging have been described in the literature [13–16]. An elastic silicon manual ventilation bag (SilkoBag, Ruesch, Erlangen, Germany) with a volume of 500 ml served as a lung phantom [12]. This phantom was connected to an intensive-care-type mechanical ventilator (Servo 900 C, Siemens Medical Solutions, Erlangen, Germany) and a microprocessor-controlled gas delivery device (US and international patent no. PCT/EP98/07516). The ventilator was set to administer a tidal volume of 406 ± 1 ml at 13 cycles per minute in a constant-flow and volume-controlled ventilation mode. For measurements, 59 ± 24 ml hyperpolarized ^{3}He (degree of polarization approximately 55%) was introduced as the initial portion of the tidal volume. Imaging was performed during a manual inspiratory ventilation hold, using a double-acquisition algorithm as described previously [10–12, 17]. For reference measurement, respiratory gas analysis was performed using a freshly calibrated side-stream respiratory gas analyzer (Capnomac Ultima, Datex, Helsinki, Finland). Gas analysis was performed immediately after imaging to avoid gas motion artifacts.

Several PO_2 levels in the normoxic and hypoxic range were produced by mixing nitrogen with room air. The tidal volumes delivered by the respirator and the amount of ^{3}He administered for paired acquisitions were measured and reproduced as exactly as possible.

Imaging was performed with a 1.5-T whole-body scanning system (Magnetom Vision, Siemens Medical Solutions, Erlangen, Germany) equipped with a broadband amplifier and a double-resonant coil (Fraunhofer Institut, St. Ingbert, Germany) to measure at the Larmor frequency of ^{3}He (48.5 MHz). The following measurements were performed:

1. 2D measurements using a pulse sequence as validated in previous studies [12] (coronal orientation; repetition time, TR, 11.0 ms, echo time, TE, 4.2 ms, α 2.7°; bandwidth 163 Hz/pixel, no slice selection; acquisition matrix 81×128; field of view, FoV, 320 mm; resolution 3.95×2.5 mm; time of acquisition 1 s).
2. 3D measurements using a 3D spoiled gradient echo pulse sequence (coronal orientation; TR 3.8 ms, TE 1.3 ms, α 0.5°; bandwidth 488 Hz/pixel, number of partitions 16; acquisition matrix 44×128; FoV 500 mm; resolution 5.68×3.91 mm; time of acquisition 2.7 s).

Centric phase encoding was used in 2D sequences, centric reordering in the phase encoding direction and linear phase order in slice directions in 3D sequences. Sinc interpolation was used in all three directions to result in a final matrix size of 256×256 for 2D and 256×128×32 with a rectangular field of view of 4/8 for 3D measurements. The reconstructed partition thickness was 15.6 mm. Each sequence was performed in a double-acquisition mode with a short (2D, τ_1=1 s; 3D, τ_1=2.7 s) and a long (2D and 3D, τ_2=4.0 s) interscan interval to mathematically exclude the effect of radio frequency pulsing from that of molecular oxygen in the analysis of serial images [10, 17]. All other imaging parameters were kept constant within the pulse sequence. Each acquisition comprised a series of eight single images obtained during one inspiratory hold, with side-stream test gas suction of the gas analyzer either turned off or—for selected measurements—turned on at a flow rate of 200 mL/min.

Measurements were performed at several differently equilibrated oxygen concentrations:

1. 0% (corresponding to a PO_2 of 0.00 bar)
2. 6% (corresponding to a PO_2 of 0.06 bar)
3. 10% (corresponding to a PO_2 of 0.10 bar)
4. 13% (corresponding to a PO_2 of 0.13 bar)
5. 20.9% (room air, corresponding to a PO_2 of 0.21 bar)
6. 0.0 and 20.9% with ongoing gas suction (200 mL/min) via the respiratory gas analyzer to mimic a continuous volume loss of the "model alveolus" during incomplete inspiratory hold in vivo, e.g., by slow expiration

These preset oxygen concentrations were, of course, diluted by the instantaneous addition of the ^{3}He gas just prior to imaging and consecutive gas analysis.

Image analysis

Images were postprocessed on a personal computer, using self-developed software based on PV-WAVE (Visual Numerics, Boulder, Colorado, USA). Calculation of $P_{He}O_2$ based on the decay of the signal intensity ($A_{0...n}$) in n serial images during O_2 exposures, i.e., inflation holds, of different duration [$\tau_1(n-1)$ or $\tau_2(n-1)$] follows the relationship

$$\ln\left(\frac{A_n}{A_0}\right)(\tau_1) - \ln\left(\frac{A_n}{A_0}\right)(\tau_2) = f(PO_2)$$

and has been described before [18]. Noise correction according to the method of Gudbjartsson [19] was applied. Images with insufficient signal-to-noise ratio (SNR) (SNR<3) were excluded from analysis [20].

The software provides automatic detection of ^{3}He-tagged airspace, and calculates $P_{He}O_2$ either region-of-interest-based or pixel-by-pixel-based to allow for parameter mapping. Further details are beyond the scope of this publication and the reader is referred to the dedicated literature [21, 22]. In order to limit the noise of the $P_{He}O_2$ maps, pixels were averaged over a 4×4 neighborhood, yielding a final matrix size of 64×64 for 2D and 64×32 for 3D images, respectively. Mean $P_{He}O_2$ values and their standard deviations, as well as the mean oxygen shift rate RO_2 values for a linear temporal change of $P_{He}O_2$ and their standard deviations, were calculated in all ^{3}He-containing slices for the various

oxygen concentrations. For 3D measurements, median values for each measurement (over all acquired slices) were determined. A slice profile was calculated by subtraction of the mean for all slices combined from each mean of the respective slice.

Results

2D measurements

Preset oxygen concentrations were modified by the amount of ^{3}He gas introduced into the phantom. Thus, the respective O_2-sensitive ^{3}He measurements were performed within an atmosphere containing 0.000, 0.066, 0.100, 0.134, and 0.195 bar PO_2 at constant bag volume as determined by the gas analyzer after image acquisition. The measured PO_2 values during image acquisitions with ongoing gas loss of 200 mL/min were 0.000 and 0.192 bar, respectively. The median SNR in the first image of each series was 27.8 (range 11.2–81.5) (Fig. 1a, cf. Fig. 1b). Nevertheless, the last two images of the acquisition with long interscan interval τ at 0.100 bar PO_2 had insufficient SNR (SNR<3) and were excluded from postprocessing together with the two corresponding images of the respective acquisition with short τ.

Figure 2a shows the comparison between gas analysis and 2D ^{3}He-MRI-based $P_{He}O_2$ measurements in the constant-volume lung phantom (Pearson's correlation coefficient r=0.98, correlation for all 2D measurements r=0.96). The measurements had a mean bias of −0.027 and precision limits from −0.056 to 0.002 (Fig. 3a). Thus, there is a small systematic overestimation of PO_2 by ^{3}He-MRI. The mean oxygen shift rate RO_2 in the constant-volume phantom was found to range from 0.03 to −1.19 mbar/s, indicating a trend to decreasing $P_{He}O_2$ during inflation hold; however, this rate was not found to differ significantly from 0 (p>0.1).

There was no statistical association between the observed decrease in the rate and the $P_{He}O_2$ measured by 2D ^{3}He-MRI (Fig. 4a). The oxygen shift rate in the phantom with ongoing gas suction was 0.30 mbar/s at 0.000 bar and 0.98 mbar/s at 0.192 bar PO_2, indicating increasing $P_{He}O_2$ during inflation hold.

3D measurements

The respective 3D measurements were performed at 0.000, 0.068, 0.107, 0.134, and 0.197 bar in the constant-volume bag as determined by the gas analyzer, and at 0.188 bar with gas loss from the bag at 200 mL/min. The 3D images had lower SNR compared with the 2D images (first images of each series, mean 14.0, standard deviation 8.1). Thus, the SNR was insufficient (less than 3) in the last image of three series and in the last two images of two other series and the corresponding values were excluded from $P_{He}O_2$ calculation (Fig. 1b). In all but one series, the SNR of the two most peripheral signal-containing slices was also insufficient, requiring exclusion of these images from the evaluation.

Figure 2b shows the respective comparison of the O_2-sensitive ^{3}He-MRI with the conventional measurements. Pearson's correlation coefficient was r=0.89 for constant-volume measurements, and r=0.9 for all 3D measurements. There was a mean bias of −0.0043 and the precision limits were from −0.075 to 0.067 (Fig. 3b).

A slice profile of the measurements illustrates that slices close to the center produce quite consistent values, whereas slices at the periphery show a systematic drift to higher values.

The oxygen change rate RO_2 was measured to be between 1.6 and −4.4 mbar/s in the constant-volume phantom. The medians of the RO_2 decrease drifted to more negative values at higher $P_{He}O_2$ measured by 3D ^{3}He-MRI (Fig. 4b).

Fig. 1 **a** 2D image set of a lung phantom with 1-s (*upper row*) and 4-s (*lower row*) interscan interval. Measurement with room air. The difference in signal loss between the two series is easily depicted. **b** Typical 3D image set of medial slices of the lung phantom with 2.7-s (*upper row*) and 4-s (*lower row*) interscan interval. Measurement with room air. The signal-to-noise ratio is markedly lower when compared with 2D measurements. The signal-to-noise ratio in the last image of each series is insufficient; such images were excluded from evaluation.
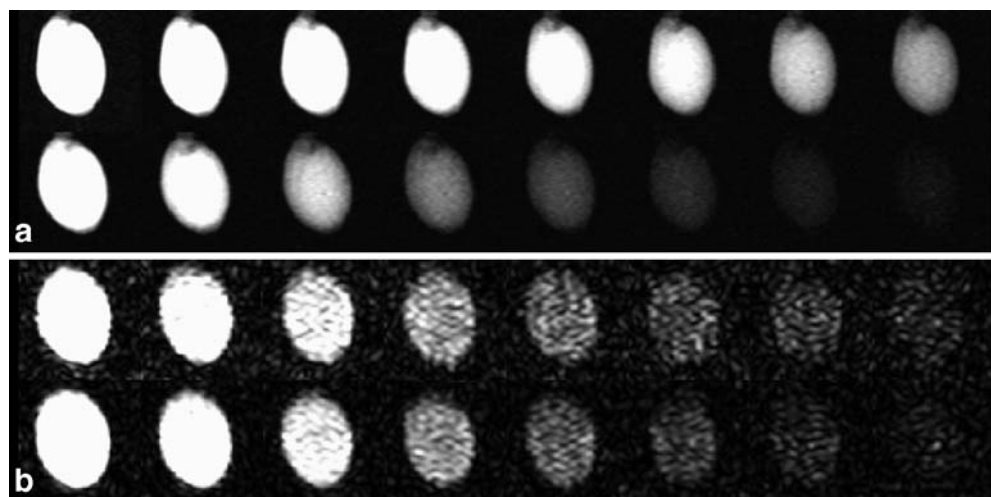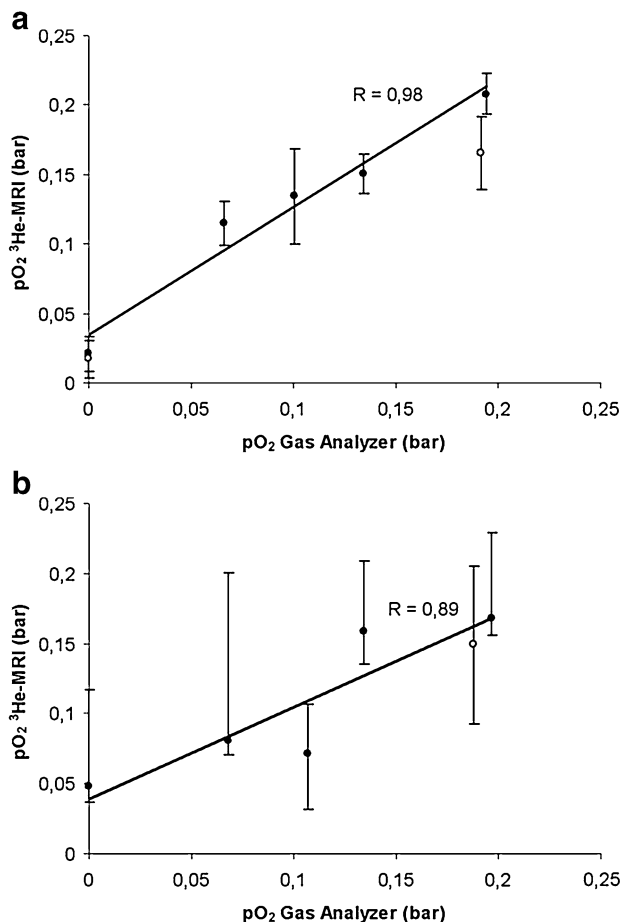
Fig. 2 a Correlation of the $P_{He}O_2/PO_2$ determinations by 2D oxygen-sensitive ^{3}He-MRI and gas analysis. *Filled dots* constant-volume phantom; *open dot* phantom with gas loss of 200 mL/min during image acquisition. *Dots* and *error bars* show the mean and the standard deviation of the mapped $P_{He}O_2$ distribution, respectively. Regression analysis excludes values measured during constant gas depletion. **b** Correlation of the $P_{He}O_2/PO_2$ determinations by 3D oxygen-sensitive ^{3}He-MRI and gas analysis. At a correlation of as good as 0.9 very low values seem to be overestimated, higher values underestimated. *Dots* and *errors bars* show the median and the range of all slices containing the ^{3}He signal. Regression analysis excludes values measured during constant gas depletion.

Discussion

Image-based and, hence, spatially resolved determination of gas-phase $P_{He}O_2$ using oxygen-sensitive ^{3}He-MRI was validated in this study, using an already published 2D pulse sequence and a 3D pulse sequence in a simple lung phantom. Conventional respiratory gas analysis was used as a reference. Six different oxygen concentrations ranging between anoxic gas and normal dry room air served for validation; this covers the full range of physiologically and pathologically occurring levels of alveolar PO_2 in mammals breathing air.
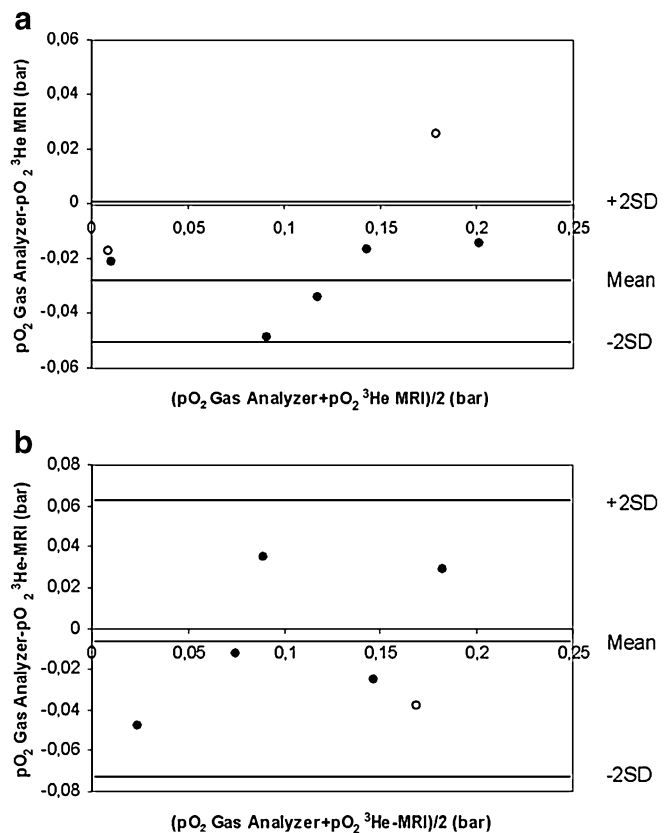

Fig. 3 a Constant-volume (*filled dots*) and "gas-exchange" (*open dot*) Bland–Altman plot for the regression in Fig. 2a with a slightly negative median bias and a range of measurement results. **b** Bland–Altman plot for the regression in Fig. 2b. 3D measurements show a slightly positive median bias; the absolute range of measurement errors is on the order of that of the 2D measurement. The Bland–Altman analyses in **a** and **b** exclude gas-exchange values.

Oxygen partial pressure $P_{He}O_2$

Currently, most ^{3}He-MR image-based $P_{He}O_2$ measurements use 2D pulse sequences [10, 17, 23] with or without slice selection. 2D sequences offer sufficient SNR and in-plane resolution and yield robust measurements [17, 18]. The SNR in the newly introduced 3D measurement was only about half of that obtained in 2D imaging. When sequence parameters are kept constant 3D images have 4 times the signal intensity of 2D images [24]. In the present study though, the slice thickness was not constant as the 2D sequence omits slice selection whereas the 3D sequence yields a considerable improvement in spatial resolution. A partition thickness of 15 mm still appears less than optimal with regard to lung structure and the dimensions of pulmonary acini, i.e., the functional units of the lung, but it already approaches the limit of spoiled gradient echo sequences, as used in the present study. However, superimposition of regions with different PO_2 is already reduced
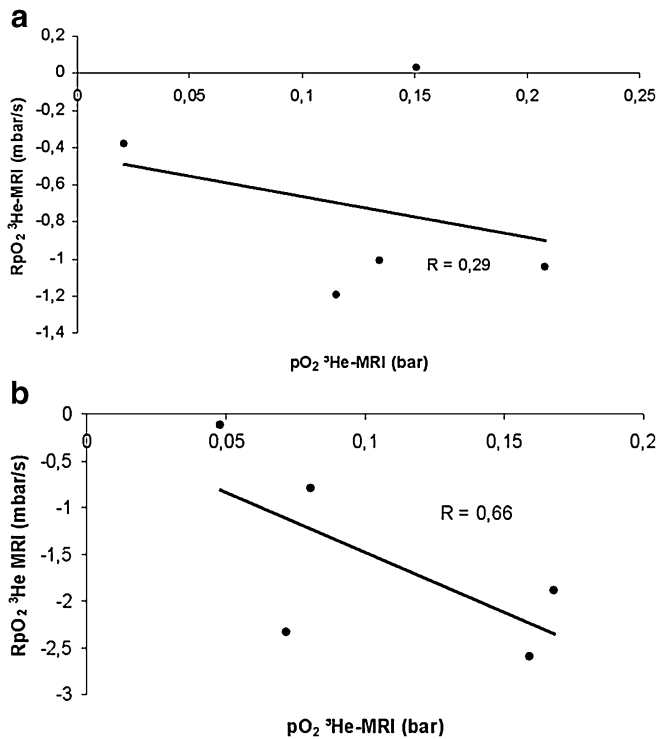
Fig. 4 Rate of oxygen decrease during inspiratory inflation hold against $P_{He}O_2$ measured by [3]He-MRI. **a** 2D measurements show no correlation with $P_{He}O_2$. Although the correlation in 3D measurements (**b**) is not strict, higher oxygen concentrations tend to produce higher errors in the oxygen decrease rate as no oxygen consumption is expected in a phantom.

substantially when compared with measurements without slice selection. Administration of sufficiently high [3]He degrees of polarization thus becomes crucial in 3D measurements to obtain sufficient SNR.

The 2D series demonstrate a good and practically useful correlation between measurements, with a small systematic overestimation of PO_2 by [3]He-MRI. In 3D measurements, correlation with conventional gas analysis is a little less strong, but is still close to 0.9. Nevertheless, the standard deviation of the results of the 3D measurements within a single partition is larger, which is probably due to the lower SNR of the source images. Another two potential error sources may explain why the results obtained from 2D and 3D measurements vary slightly. First, in 2D measurements, the difference between τ_1 and τ_2 is 3 s (τ_1=1 s vs. τ_2=4 s), whereas in 3D measurements it is only 1.3 s (τ_1=2.7 s vs. τ_2=4 s), owing to the longer imaging time required for 3D imaging. This leads to a poorer discrimination between the signal-destroying effects from high-frequency pulsing and oxygen. Second, in 3D measurements more images had to be excluded from the image analysis owing to the low SNR. This leaves fewer images for $P_{He}O_2$ calculation in the 3D imaging series. However, Bland–Altman analysis (Fig. 3b) shows deviations from the gas analysis for the 3D

measurements which are comparable to those of the 2D measurements.

The partition profile of the 3D measurements showed increasing inaccuracy for slices at the periphery of the phantom. Falsely high $P_{He}O_2$ values may have been determined in these partitions for several reasons. The long respiratory tubing required for inflation and deflation of the phantom inside the scanner increases the chance of gas leakage from the circuit and, hence, gas redistribution from the phantom into the tubing during the measurement. This may cause the phantom to shrink slightly during MRI acquisition, which in turn would move parts of the phantom out of peripheral partitions and thus accelerate apparent signal decay. Also, in a phantom or other structure with very smooth edges, partial volume averaging becomes a source of error in peripheral partitions. Although correlation was only marginally different after omitting these partitions, it is recommended to neglect images in the $P_{He}O_2$ calculation which contain significant partial volume averaging.

2D measurements slightly overestimated conventional PO_2 measurement, whereas data acquired during a constant gas loss of 200 mL/min from the phantom by test gas aspiration tended to decrease the overestimation or underestimated PO_2. In numerical simulations of the double-acquisition setup, the superimposition of a constant gas signal loss from the volume of interest and two exponential signal decays (from oxygen and radio frequency excitation) led to a nonlinear decrease in apparent [3]He-based PO_2 measurements, depending on the rate of the linear loss. This explains most of the "reversed" bias observed in our 2D experiments with constant-flow gas aspiration. Nevertheless, since signal loss due to gas leakage might be nonlinear or cause premature attrition of the SNR, any respiratory movement or intrapulmonary "pendelluft" will affect measurement of oxygen relaxation in a largely unpredictable way. Shrinkage of the phantom would only influence the signal intensity of the peripheral partitions or the margins of the phantom in the central partitions, as the gas concentration and the partition volume containing [3]He signal remain fairly constant. Consequently, peripheral partitions in 3D measurements and 2D measurements tend to misinterpret $P_{He}O_2$ in the same sense. Thus, in general, 3D analysis appears more robust against the effects of superimposed gas volume losses from the volume of interest.

Error sources independent of the type of imaging sequence are, e.g., spin relaxation by surface properties of the bag or small errors in barometric measurements and ventilator circuit pressure determination. Since comparable silicon bags have relaxation times of 40–50 min [12], a significant influence by the bag's surface relaxation seems unlikely. The total errors of atmospheric pressure measurement within the bag are safely assumed to be less than 20 mbar and would therefore account for a bias of only less than 2% of the assumed true PO_2, which is not large enough to fully explain the observed bias. The observed bias of the $P_{He}O_2$ is also close to the measurement errors of the O_2

analyzer system, which are given by the manufacturer as less than 2% of the full measurement scale. Thus, this may well contribute to systematic errors in the observed range of 1.7% O_2.

Oxygen exchange rate RO_2

As there was no oxygen consumption during the measurements, a tendency to overestimate the oxygen decrease rate RO_2 cannot be fully excluded, although there was no statistically significant difference from 0 in 2D measurements. In 3D measurements, there appeared to be a correlation between the measured $P_{He}O_2$ and the measured RO_2, in the sense that higher $P_{He}O_2$ levels produced higher oxygen decrease rates. As measurements at higher PO_2 in general show a lower SNR owing to the signal destruction by molecular oxygen, it is likely that the SNR influences the results of RO_2 significantly. Thus, measurements of oxygen decrease by 3D measurements seem critical under the observed circumstances. 2D measurements did not show this kind of relationship. However, there might still be some convective gas movement following the inflation of the phantom to the peak inspiratory pressure, which would take place, for a short duration, right at the beginning of the measurement. The ceasing of convection could then decrease the intensity of contact between ^{3}He atoms and paramagnetic oxygen molecules over the measurement period, which may result in decelerating the relaxation and thus, decrease of "apparent PO_2" over time.

These mechanisms discussed for the large phantom alveolus are not entirely transferable to the human lung, where convective gas transport only takes place in the central airways and restricted diffusive motion should be the only gas transport mechanism in inspiratory breath hold.

Spatial resolution of the $P_{He}O_2$ maps appears limited when the resolution of the source images has to be further reduced. However, spatial resolution as in computed tomography is not essential for oxygen mapping. If spatial resolution of the maps can be improved to that of the source images with further optimization of the SNR, oxygen partial pressure maps yield spatial resolution which may approach the dimensions of the functional respiratory units of the lung.

Recently, there have been publications on pulmonary ventilation and perfusion imaging using ^{3}He-MRI with intravenous application of paramagnetic gadolinium contrast medium or by combination of ^{3}He-MRI and proton MRI [25, 26]. Since the PO_2 in the lung is a result of the balance between ventilation and perfusion, determination of the V/Q ratio is feasible with knowledge of the oxygen–hemoglobin binding curve. Thus, oxygen-sensitive ^{3}He-MRI may develop into a rapid noninvasive technique to scan for regional ventilation/perfusion mismatch, where appropriate supported by other ^{3}He-MRI modalities to clarify the sources of mismatch [27–31].

Conclusion

2D and 3D oxygen-sensitive ^{3}He-MRI is an evolving method to noninvasively map the regional distribution of oxygen partial pressure in gas-filled spaces.

2D projection measurements are robust but are limited by superimposition. 3D measurements can reduce this shortcoming markedly but require exact application of highly polarized gas to yield sufficient SNR. This approach allows for spatially resolved oxygen partial pressure mapping which may, with further optimization of the SNR, approach the dimensions of the functional respiratory units of the lung.

References

1. McAdams HP, Palmer SM, Donnelly LF, Charles HC, Tapson VF, MacFall JR (1999) Hyperpolarized 3He-enhanced MR imaging of lung transplant recipients: preliminary results. Am J Roentgenol 173:955–959

2. Kauczor HU, Hofmann D, Kreitner KF, Nilgens H, Surkau R, Heil W, Potthast A, Knopp MV, Otten EW, Thelen M (1996) Normal and abnormal pulmonary ventilation: visualization at hyperpolarized He-3 MR imaging. Radiology 201(2):564–568

3. Guenther D, Eberle B, Hast J, Lill J, Markstaller K, Puderbach M, Schreiber WG, Hanisch G, Heussel CP, Surkau R, Grossmann T, Weiler N, Thelen M, Kauczor HU (2000) (3)He MRI in healthy volunteers: preliminary correlation with smoking history and lung volumes. NMR Biomed 13:182–189

4. Altes T, Powers P, Knight-Scott J, Rakes G, Platts-Mills T, de Lange E, Alford B, Mugler JI, Brookeman J (2001) Hyperpolarized 3He MR lung ventilation imaging in asthmatics: preliminary findings. J Magn Reson Imaging 13:378–384

5. van Beek EJ, Schmiedeskamp J, Wild JM, Paley MN, Filbir F, Fichele S, Knitz F, Mills GH, Woodhouse N, Swift A, Heil W, Wolf M, Otten E (2003) Hyperpolarized 3-helium MR imaging of the lungs: testing the concept of a central production facility. Eur Radiol 13(12):2583–2586

6. Eibel R, Weber A, Stolpe S, Hellenbrand U, Bauer T (2002) Zusammenhang zwischen Empyhsemtyp und Schweregrad der Pneumokoniose bei Bergleuten: Korrelation von HR-CT-Befunden und ILO-Klassifikation [Correlation of different types of emphysema in high-resolution computed tomography (HR-CT) with the ILO-classification of coal workers pneumoconiosis]. Fortschr Röntgenstr 174:846–853

7. Kauczor HU, Ebert M, Kreitner KF, Nilgens H, Surkau R, Heil W, Hofmann D, Otten EW, Thelen M (1997) Imaging of the lungs using 3He MRI: preliminary clinical experience in 18 patients with and without lung disease. J Magn Reson Imaging 7(3):538–543

8. Gast KK, Ley S, Zaporozhan J, Puderbach M, Eberle B, Biedermann A, Knitz F, Schmiedeskamp J, Weiler N, Schreiber W, Mayer E, Heussel C, Thelen M, Kauczor H (2003) Reformatierungen als Lösungsansatz für die Problematik der unterschiedlichen Schichtführung beim Vergleich von ^{3}He-MRT und HR-CT der Lunge [Reformation as proposed solution for the problem of sectioning different levels with 3He-MRT and HR-CT of the chest]. Fortschr Röntgenstr 175:786–790

9. Kauczor HU, Ebert M, Kreitner KF, Grossmann T, Nilgens H, Hofmann D, Surkau R, Roberts T, Heil W, Otten EW, Thelen M (1997) Helium-3-MRT der Lungenventilation: Erste klinische Anwendungen [The helium-3 MRT of pulmonary ventilation: the initial clinical applications]. Fortschr Röntgenstr 166(3):192–198

10. Eberle B, Weiler N, Markstaller K, Kauczor H, Deninger A, Ebert M, Grossmann T, Heil W, Lauer LO, Roberts TP, Schreiber WG, Surkau R, Dick WF, Otten EW, Thelen M (1999) Analysis of intrapulmonary O(2) concentration by MR imaging of inhaled hyperpolarized helium-3. J Appl Physiol 87(6):2043–2052

11. Deninger AJ, Eberle B, Ebert M, Grossmann T, Hanisch G, Heil W, Kauczor HU, Markstaller K, Otten E, Schreiber W, Surkau R, Weiler N (2000) (3)he-MRI-based measurements of intrapulmonary p(O2) and its time course during apnea in healthy volunteers: first results, reproducibility, and technical limitations. NMR Biomed 13(4):194–201

12. Eberle B (2000) Development and implementation of a new method to determine the regional partial pressure of O2 in the lung and its time course during apnea. Experimental and clinical studies with ^{3}He-MRI., in Habilitation Thesis, Department of Anesthesiology. Johannes Gutenberg-University: Mainz, Germany

13. Colegrove FD, Schearer LD, Walters K (1963) Polarization of ^{3}He gas by optical pumping. Phys Rev 132:2561–2572

14. Becker J, Heil W, Krug B, Leduc M, Meyerhoff M, Nacher P, Otten EW, Prokscha T, Schearer LD, Surkau R (1994) Study of mechanical compression of spin-polarized 3He gas. Nucl Instrum Methods A 346:45–51

15. Eckert G, Heil W, Meyerhoff M, Otten EW, Surkau R, Werner M, Leduc M, Nacher PJ, Schearer LD (1992) A dense polarized 3He target based on compression of optically pumped gas. Nucl Instrum Methods Phys Res A 320:53–65

16. Schad LR, Bachert P, Bock M, Essig M, Knopp MV, Ebert M, Grossmann T, Heil W, Surkau R, Otten EW (1997) Hyperpolarized gases—a new type of MR contrast agents? Acta Radiol Suppl 412:43–46

17. Deninger A, Eberle B, Bermuth J, Escat B, Markstaller K, Schmiedeskamp J, Schreiber W, Surkau R, Otten E, Kauczor H-U (2002) Assessment of a single-acquisition imaging sequence for oxygen-sensitive 3He MRI. Magn Reson Med 47:105–114

18. Deninger AJ, Eberle B, Ebert M, Grossmann T, Heil W, Kauczor H, Lauer L, Markstaller K, Otten E, Schmiedeskamp J, Schreiber W, Surkau R, Thelen M, Weiler N (1999) Quantification of regional intrapulmonary oxygen partial pressure evolution during apnea by (3)He MRI. J Magn Reson 141(2):207–216

19. Gudbjartsson H, Patz S (1995) The Rician distribution of noisy MRI data. Magn Reson Med 34(6):910–914. Erratum in: Magn Reson Med 1996 Aug;36(2):332

20. Schreiber WG, Eberle B, Laukemper-Ostendorf S, Markstaller K, Weiler N, Scholz A, Burger K, Heussel C, Thelen M, Kauczor H (2001) Dynamic (19) F-MRI of pulmonary ventilation using sulfur hexafluoride (SF(6)) gas. Magn Reson Med 45(4):605–613

21. Lehmann F, Eberle B, Markstaller K, Gast KK, Schmiedeskamp J, Blümler P, Kauczor HU, Schreiber WG (2004) Ein Auswerteprogramm zur quantitativen Analyse von Messungen des alveolären Sauerstoffpartialdrucks (pAO2) mit der sauerstoffsensitiven 3He-MR-Tomographie [A Software Program for Quantitative Analysis of Alveolar Oxygen Partial Pressure (pAO2) with Oxygen-sensitive 3He-MRI]. Fortschr Röntgenstr 176(10):1390–1398

22. Lehmann F, Knitz F, Weiler N, Gast KK, Ley S, Schmiedeskamp J, Bellemann ME, Kauczor HU, WG Schreider (2004) Quantitative Untersuchung der Lungenventilation mittels dynamischer MRT von hochpolarisiertem Helium-3 [A Software Tool for Analysis and Quantification of Regional Pulmonary Ventilation Using Dynamic Hyperpolarised-3He-MRI]. Fortschr Röntgenstr 176(10):1399–1408

23. Moeller H, Hedlund L, Chen X, Carey M, Chawla M, Wheeler C, Johnson G (2001) Measurements of hyperpolarized gas properties in the lung. Part III: 3He T1. Magn Reson Med 45:421–430

24. Wild JM, Woodhouse N, Paley MN, Fichele S, Said Z, Kasuboski L, van Beek EJR (2004) Comparison between 2D and 3D gradient-echo sequences for MRI of human lung ventilation with hyperpolarized 3He. Magn Reson Med 52:673–678

25. Rizi RR, Saha PK, Wang B, Ferrante MA, Lipson D, Baumgardner J, Roberts DA (2003) Co-registration of acquired MR ventilation and perfusion images-validation in a porcine model. Magn Reson Med 49(1):13–18

26. Rizi RR, Lipson DA, Dimitrov IE, Ishii M, Roberts DA (2003) Operating characteristics of hyperpolarized 3He and arterial spin tagging in MR imaging of ventilation and perfusion in healthy subjects. Acad Radiol 10(5):502–508

27. Gast KK, Viallon M, Eberle B, Lill J, Puderbach M, Hanke A, Schmiedeskamp J, Kauczor H-U (2002) MR imaging in lung transplant recipients using hyperpolarized 3He: comparison with CT. J Magn Reson Imaging 15:268–274

28. Gast KK, Puderbach M, Rodriguez I, Eberle B, Markstaller K, Knitz F, Schmiedeskamp J, Weiler N, Schreiber W, Mayer E, Thelen M, Kauczor H (2003) Distribution of ventilation in lung transplant recipients: evaluation by dynamic ³He-MRI with lung motion correction. Invest Radiol 38:341–348

29. Gast KK, Zaporozhan J, Ley S, Biedermann A, Knitz F, Eberle B, Schmiedeskamp J, Heussel CP, Mayer E, Schreiber WG, Thelen M, Kauczor HU (2004) ³He-MRI in follow-up of lung transplant recipients. Eur Radiol 14:78–85

30. Ley S, Zaporozhan J, Morbach A, Eberle B, Gast KK, Heussel C-P, Biedermann A, Mayer E, Schmiedeskamp J, Stepniak A, Schreiber WG, Kauczor H-U (2004) Functional evaluation of emphysema using diffusion-weighted 3Helium-magnetic resonance imaging, high-resolution computed tomography, and lung function tests. Invest Radiol 39 (7):427–434

31. Salerno M, Altes TA, Brookeman JR, De Lange EE, Mugler JP III (2001) Dynamic spiral MRI of pulmonary gas flow using hyperpolarized ³He: preliminary studies in healthy and diseased lungs. Magn Reson Med 46:667–677